White Rose Research Online
eprints@whiterose.ac.uk
https://eprints.whiterose.ac.uk
Universities of Leeds, Sheffield and York

Deposited via The University of Sheffield.

White Rose Research Online URL for this paper:
https://eprints.whiterose.ac.uk/id/eprint/238571/

Version: Accepted Version

Article:

Niu, C., Chen, B., Smith, E. et al. (2026) Image-based metrics for characterizing drilling induced defects in fibre-reinforced composite. IEEE Transactions on Instrumentation and Measurement. ISSN: 0018-9456

https://doi.org/10.1109/tim.2026.3667285

© 2026 The Authors. Except as otherwise noted, this author-accepted version of a journal article published in IEEE Transactions on Instrumentation and Measurement is made available via the University of Sheffield Research Publications and Copyright Policy under the terms of the Creative Commons Attribution 4.0 International License (CC-BY 4.0), which permits unrestricted use, distribution and reproduction in any medium, provided the original work is properly cited. To view a copy of this licence, visit http://creativecommons.org/licenses/by/4.0/

Reuse
This article is distributed under the terms of the Creative Commons Attribution (CC BY) licence. This licence allows you to distribute, remix, tweak, and build upon the work, even commercially, as long as you credit the authors for the original work. More information and the full terms of the licence here: https://creativecommons.org/licenses/

Takedown
If you consider content in White Rose Research Online to be in breach of UK law, please notify us by emailing eprints@whiterose.ac.uk including the URL of the record and the reason for the withdrawal request.

UNIVERSITY OF LEEDS
University of Sheffield
UNIVERSITY of York

Image-based Metrics for Characterizing Drilling Induced Defects in Fibre-Reinforced Composite

Chaoyue Niu[1], Bin Chen[1*], Erica Smith[2], Robert Bramley[2], Oliver Hayes[2], Pete Crawforth[2], Kevin Kerrigan[2], Mahdi Mahfouf[1] and Visakan Kadirkamanathan[1]

***Abstract*—Modern aircraft assembly involves drilling holes in multi-material stacks, followed by fastening to create a structural joint. Stringent quality requirements to ensure structural integrity necessitate accurate assessment of the hole quality. Carbon fibre reinforced polymer (CFRP) is widely used in aircraft structures, and delamination and uncut fibres are prominent defects associated with CFRP drilling. Furthermore, metal-CFRP composite structures, owing to their higher cost and hence the need reduced waste, present even more stringent requirements on hole quality. Defects such as delamination and uncut fibres in this composite also differ in how they manifest. An automated evaluation framework and robust hole quality metrics are therefore required to address this challenge. In this paper, an automated image processing based evaluation framework for rapid and objective assessment of delamination and uncut fibre defects is developed. This robust framework introduces combined metrics, leveraging a weighted p-norm approach to aggregate five factors for delamination and five for uncut fibres with $p = 1$, 2 and ∞. A method to choose weights for the different p-norms is also identified to create robust measures. Grayscale images captured via optical microscopy serve as inputs, and the framework outputs both the combined metrics and ten individual metrics for detailed analysis. The multi-objective space with the associated Pareto front and population based ranking derived from the weighted p-norm based metrics are introduced as a means to identify relative hole quality and to associate these with the machining parameters. A dataset comprising 24 holes from two metal-CFRP composite workpieces produced in a robotic drilling operation is used for demonstration of the framework. The results demonstrate the effectiveness of the proposed framework and its utility for real-world applications.**

***Index Terms*—Robotic Drilling; Metal-CFRP Composite; Hole Defects Assessment; Optical Metrology; Vision-Based Inspection.**

I. INTRODUCTION

Aircraft assembly relies heavily on fasteners fitted into precisely drilled holes to ensure structural integrity and secure component connections. Each year, hundreds of millions of holes are drilled in aircraft structures, all of which must meet stringent quality standards to guarantee a proper fit for fasteners and maintain the overall durability of the joints. However, achieving these quality requirements presents significant challenges. Factors such as multi-material components, dynamic instability in robotic drilling systems, and the need to meet high production rates can compromise hole quality and make it difficult to ensure compliance with specifications.

Carbon Fiber Reinforced Polymer (CFRP) composites are widely used in aerospace applications as their useful properties, including their high strength-to-weight ratios and resistance to corrosion [1], [2]. However, CFRP drilling introduces unique challenges, as the material is prone to defects such as uncut fibres and delamination [3], [4]. Ensuring part quality during drilling remains a critical concern in manufacturing. Methods such as in-process error compensation [5] and probabilistic frameworks [6] have been explored, but the measurement and prediction of such defects remain open challenges. Evaluating these defects is thus essential for optimizing aircraft assembly processes and enhancing performance and safety.

Existing research on CFRP drilling [7]–[10] has primarily focused on assessing delamination damage by considering factors such as crack length and delamination area. However, these studies often overlook the influence of uncut fibres within the hole, which are equally problematic as they interfere with the proper fitting of fasteners. Empirical studies [11], [12] have shown that uncut fibres occur with a frequency similar to delamination in CFRP drilling. When layers delaminate, structural integrity can be compromised, causing fibres to deflect under cutting forces instead of being cleanly cut, leading to the formation of uncut fibres. Voß et al. [13] proposed a unified characteristic that combines delamination and uncut fibre parameters for assessing hole quality. Their approach included two delamination factors and three uncut fibre factors but left room for a more comprehensive evaluation. While numerous metrics for assessing hole quality have been proposed and proven effective in specific studies, there remains a lack of consensus regarding standardized and reliable metrics for comprehensive defect evaluation. The existing literature on CFRP hole defects bring with them their own assumptions, resulting in an uncertainty over which metrics are most suitable.

Several techniques for measuring delamination and uncut fibres have been presented in the literature, including light optical microscopy, scanning electron microscopy, and ultrasonic C-scan [13]–[15]. Manual evaluation of raw inspection data introduces additional challenges, including subjectivity and inefficiency. In contrast, vision-based methods [16], [17] have gained considerable attention for industrial defect in-

---

[1] Chaoyue Niu, Bin Chen, Mahdi Mahfouf & Visakan Kadirkamanathan are with School of Electrical and Electronic Engineering, University of Sheffield, UK. (email: {c.niu,bin.chen,m.mahfouf,visakan}@sheffield.ac.uk; [2] Erica Smith, Robert Bramley, Oliver Hayes, Pete Crawforth & Kevin Kerrigan are with Advanced Manufacturing Research Centre (AMRC), University of Sheffield, UK. (email: {erica.smith,r.bramley, o.hayes,p.crawforth,k.kerrigan}@amrc.co.uk.

This work was supported by the UK Engineering and Physical Sciences Research Council EP/P006930/1 and Innovate UK project 113347 through High Value Manufacturing Catapult funding. The trials were supported by AMRC members: Yousef Bhaker, Michael Garrett, Sean Delaney, Luke Rutter, Lucy Mello, Emma Warren, Andrew Oakley and John Carmichael.

*The corresponding author: bin.chen@sheffield.ac.uk.

spection due to their speed and reliability. Digital image processing techniques [18], particularly at the pixel level using high-resolution images, offer a promising solution for the quantitative analysis of defects. These methods enable rapid inspection by identifying and tallying defect-associated pixels and provide precise pixel coordinate data, simplifying the detection of irregularities around drilled holes.

Current research on drilled-hole quality in CFRP covers physics-based modelling, traditional non-destructive testing (NDT), and increasingly, vision- and data-driven image analysis [19], but important gaps remain that motivate the present work. Foundational studies established the mechanical origins of drilling-induced delamination and related metrics for quantifying exit/entry damage (e.g., analytical treatment of delamination [20]), and various delamination indices (e.g., adjusted delamination factors) have been widely used to relate machining conditions to damage severity. Digital image analysis was introduced to obtain objective, repeatable measures of delamination [9], [10], and more recent efforts have proposed unified quality measures that explicitly include uncut-fibre features alongside delamination [13], acknowledging that uncut fibres and delamination are coupled failure modes in CFRP drilling. Importantly, the extracted delamination and uncut-fibre metrics can directly be related to the structural integrity of the drilled holes, as defects such as delamination have been shown to reduce residual flexural and compressive strength in CFRP joints [4], [21], [22]. At the same time, advances in vision-based and machine-learning inspection that range from classical multi-light/thresholding pipelines to convolutional and hybrid deep models have demonstrated robust detection and segmentation of hole-edge defects under controlled imaging conditions [12], [23]. Complementary high-resolution NDT approaches, such as ultrasonic C-scan, provide volumetric confirmation of interlaminar damage but are less convenient for rapid pixel-level quantification on production lines [24]. Despite these advances, there is no broadly adopted framework that (i) integrates both length- and area-based metrics for delamination and uncut fibres, (ii) operates at pixel scale on very high-resolution imagery to capture fine uncut-fibre features, and (iii) is demonstrated with explicit computational performance assessment of its suitability for transfer to industrial settings. The need for such a framework is equally important for metal-CFRP composite stacks where the pattern of defects can be different.

This paper focuses on the development and evaluation of an image-based framework for the rapid and robust identification of two key drilling-induced defects in CFRP components of a composite stack using optical imagery. The work addresses the need for an automated and objective alternative to labour-intensive, subjective visual inspection by establishing a reproducible pipeline that extracts geometric defect metrics, aggregates them into interpretable combined scores, and produces a relative ranking of hole quality suitable for process evaluation. The study, therefore, examines (i) how image-derived metrics can reliably quantify drilling-induced defects; (ii) how multiple defect metrics can be integrated into a unified assessment method that reflects perceived hole quality; (iii) whether these combined metrics can effectively discriminate between hole quality levels, including those arising from variations in machining parameters, while supporting practical decision-making in industrial drilling and inspection workflows; and (iv) what the computational cost of the framework would be, for evaluating its feasibility for industry deployment.

The key contributions of this paper are as follows:

1) Inspired by delamination defect indices, two further metrics are introduced as measures of uncut fibre defects with an image processing pipeline involving millions of pixels with precision and accuracy.
2) A set of combined metrics based on p-norm is introduced to assess delamination damage and uncut fibre defects, incorporating *ten separate damage factors* that evaluate both length- and area-based defects.
3) Introduction of a multi-objective Pareto ranking-based evaluation of relative hole quality within the population of drilled holes and their association with machining parameters.
4) Experiments are conducted using a retrospective manufacturing trial dataset from a robotic drilling process to demonstrate the feasibility and effectiveness of the proposed metrics and image-processing framework for hole quality evaluation.

The remainder of the paper is organized as follows. Section II details the combined metrics for evaluating delamination and uncut fibre defects and introduces a novel flexible weighted-norm approach for hole quality assessment. This is followed by the development of an image-processing framework to estimate these metrics. Section III begins with a description of the test images of drilled holes, followed by the analysis of the overall performance of the combined metrics. The quality ranking of drilled holes is visualized and quantified using Pareto front plots along with their association with machining parameters. Section IV discusses the methodological contributions, practical deployment considerations, validation constraints, industrial applicability of the proposed image-based assessment framework. Section V concludes this paper and outlines future directions.

Declaration: This article is an extension of the proceedings paper [25]. Some preliminary results on the defect metrics and image processing framework have been published.

II. METHODS

A. Proposed Quality Metrics

The focus on available literature for assessing drilled hole quality of CFRP components has primarily been on delamination defects with uncut fibre defects receiving only limited attention. Analysing the available metrics for delamination defects and comparing them to the metrics of uncut fibres suggests that new metrics for uncut fibre defects can be defined in a similar manner to the delamination defects. Specifically, the delamination factors, such as F_{ed} (Index 4) and F_d (Index 1), are adapted to define two new metrics to assess the uncut fibres inside the drilled hole, complementing the existing metrics $F_{L,95\%}$, F_n, and $F_{A_{cov}}$ (Indices 7, 8 and 9) listed in Table I. The terms involved in the computation of these metrics can be found in Figure 1.

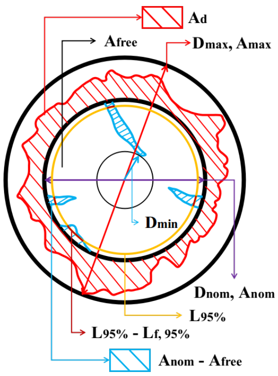

Fig. 1: Illustration of key parameters for metrics calculation. See Table I.

Drilling often results in irregularly shaped uncut fibres. The first proposed uncut-fibre factor, F_{free} (Index 10), is based on it being a proportion of an equivalent diameter value derived from the area not covered by uncut fibres to that of the nominal hole diameter. The parameter D_{free} is defined as the diameter of the circle with area A_{free}, and computed as: $D_{free} = 2\sqrt{\frac{A_{free}}{\pi}}$. The metric F_{free} is then calculated as: $F_{free} = 1 - \frac{D_{free}}{D_{nom}}$, where D_{nom} is the nominal hole diameter. This metric evaluates the presence of uncut fibres in terms of area.

The second uncut-fibre factor, F_{id} (Index 11), focuses on the minimum distance D_{min} between the center of the hole and the closest uncut fibre point. The diameter difference between the nominal diameter and the circle not covered by uncut fibres is given by: $D_{id} = D_{nom} - 2 \cdot D_{min}$. Finally, F_{id} is computed as: $F_{id} = \frac{D_{id}}{D_{nom}}$. This factor provides an indication of the length of uncut fibres in relation to the hole diameter.

The different factors aim to capture different types of defects and so a single factor may not necessarily be sufficient to characterise a particular defect. A holistic assessment of hole quality can be obtained if all the factors can be used as defect signature and then be combined into a single measure for any decision-making on whether the hole quality satisfies the requirements. Combining these factors is a challenge when their value ranges differ. Hence a transformation is applied to some of the delamination defect factors (Indices $1-4$ in Table I) such that these factors map to a range of $[0,1]$. This is achieved by using the transformation function $f(x) = 1 - e^{1-x}$ for factors with indices 1, 3, 4 and the transformation function $f(x) = 1 - e^{-x}$ for the factor with index 2. Once these metrics have all been transformed to lie in the range $[0,1]$, we can view these as multi-objective criteria as shown in Figure 2, or alternatively combined into a single measure using a weighted norm approach.

Feature Vectors and Weight Vector: Two primary feature vectors are first introduced, each representing a set of factors relevant to hole quality. Ω_{de} represents the factors associated with the metric $Q_{de} \in (0,1)$, where each component corresponds to a different characteristic of delamination. Ω_u encapsulates factors for the metric $Q_u \in (0,1)$, each representing different measure of uncut fibre defect. The weight vector $\mathbf{w} = (w_1 \;\; w_2 \;\; \cdots \;\; w_m) \in \Re^m$ where m are the number of factors being weighted, assigns weights to each factor in the respective vectors Ω_{de} and Ω_u. These are defined as:

$$\Omega_{de} = \begin{pmatrix} F'_d & F'_a & F'_{da} & F'_{ed} & F_{A_d} \end{pmatrix} \quad (1)$$

$$\Omega_u = \begin{pmatrix} F_{L,95\%} & F_n & F_{A_{cov}} & F_{free} & F_{id} \end{pmatrix} \quad (2)$$

Weighted p-norm: The p-norm [26] of a vector is a generalization of the Euclidean norm, allowing different forms of aggregation for the vector components. The weighted p-norm is used here to combine the feature components of Ω_{de} and Ω_u with their respective weights. They are defined as:

$$Q_*^{(p)} = \|\mathbf{w} \odot \Omega_*\|_p \quad \text{is the weighted } p\text{-norm} \quad (3)$$

where $\odot$ denotes the Schur product, which is an element-wise multiplication of vectors, the p-norm of the positive weight vector ($\mathbf{w} \geq \mathbf{0}$), and $*$ is a placeholder for de and u. This operation produces a new vector where each element is the product of corresponding elements from $\mathbf{w}$ and the vector of factors in (Ω_{de} or Ω_u). The parameter p determines the type of norm used, affecting how the features are aggregated. The normalisation of the weight vector needs to ensure that $Q_*^{(p)} \in [0,1]$ maps to the same range as the individual metrics, thus allowing for a suitable comparison.

Specific Forms of p-Norms: The metrics Q_{de} and Q_u are explored for different values of p, leading to distinct forms of the norm that provide various insights into the hole quality.

For $p = 1, 2, \infty$ (Weighted $1, 2, \infty$-Norm),

$$\|\mathbf{w} \odot \mathbf{z}\|_1 = w_1 z_1 + w_2 z_2 + \cdots + w_m z_m \quad (4)$$

$$\|\mathbf{w} \odot \mathbf{z}\|_2 = \sqrt{(w_1 z_1)^2 + (w_2 z_2)^2 + \cdots + (w_m z_m)^2} \quad (5)$$

$$\|\mathbf{w} \odot \mathbf{z}\|_\infty = \max\{w_1 z_1, w_2 z_2, \cdots, w_m z_m\} \quad (6)$$

The choice of the p-norms is motivated by the different degree of importance we assign to the different defect factors. If any decision about the presence of a defect is to be made from the worst outcome measure, then the use of ∞-norm is advocated. If all features are treated as providing the same amount of information for the presence of defects then the 1-norm is chosen. The 2-norm gives more importance to larger factor values whilst also allowing contribution across all factors, and thus skews the decision boundary towards more abnormal feature values.

Choice of Weights: Recognising that weights provide a balanced integration across the different factors, the unnormalised weight vector α will be chosen based on the distribution of the factor values. For each factor i (e.g., F'_d) in Ω_{de} or Ω_u, let $\mathbf{v}^{(j)}$ denote the vector of its values across jth instance (hole) and $v_i^{(j)}$ the value of the ith factor. The choice of median, mean and the mode of the distribution will be an appropriate information to be used in the choice of weights for $p = 1, 2, \infty$ respectively. To avoid the scenario of the median, mean and the mode resulting in very small values with high quality holes, a lower threshold (μ) is imposed. Hence, for $p = 1$, the choice of unnormalised weights for the i^{th} factor $\alpha_i^{(1)} = \min\{\frac{1}{\text{median}_j(\mathbf{v}_i^{(j)})}, \frac{1}{\mu}\}$; for $p = 2$, $\alpha_i^{(2)} = \min\{\frac{1}{\text{mean}_j(\mathbf{v}_i^{(j)}))}, \frac{1}{\mu}\}$; for $p = \infty$, $\alpha_i^{(\infty)} = \min\{\frac{1}{\text{mode}_j(\mathbf{v}_i^{(j)}))}, \frac{1}{\mu}\}$. The normalised weight vector associated

TABLE I: Parameters and equations for quantification of hole quality. In the "Parameter Description" column, $[\rho]$: length of one pixel; $[\rho^2]$: square area of one pixel multiplied by one pixel. See diagram illustration in Figure 1 for parameters. References are listed solely for the equation that is first proposed.

Index	Metrics	Equation	Transformed Equation	Parameter Description
Delamination (vicinity of the hole):				
1	F_d [7]	$F_d = \frac{D_{\max}}{D_{\text{nom}}}, \in [1, \infty)$	$F'_d = 1 - e^{1-F_d}, \in [0, 1)$	D_{max}: maximum diameter in delamination zone $[\rho]$; D_{nom}: nominal diameter of hole $[\rho]$.
2	F_a [8]	$F_a = \frac{A_{\text{d}}}{A_{\text{nom}}}, \in [0, \infty)$	$F'_a = 1 - e^{-F_a}, \in [0, 1)$	A_{d}: Area of delamination around vicinity of the hole $[\rho^2]$; A_{nom}: nominal circular hole area $[\rho^2]$.
3	F_{da} [9]	$F_{da} = F_d + \frac{A_d\left(F_d^2 - F_d\right)}{A_{\max} - A_{\text{nom}}}, \in [1, \infty)$	$F'_{da} = 1 - e^{1-F_{da}}, \in [0, 1)$	A_{max}: circular area of diameter D_{max} $[\rho^2]$.
4	F_{ed} [10]	$F_{ed} = \frac{1}{D_{\text{nom}}} \sqrt{\frac{4(A_d + A_{\text{nom}})}{\pi}}, \in [1, \infty)$	$F'_{ed} = 1 - e^{1-F_{ed}}, \in [0, 1)$	
5	F_{A_d} [13]	$F_{A_d} = \frac{A_d}{A_{\max} - A_{nom}}, \in (0, 1]$	-	
6	Q_{de}	$Q_{de}^{(p)} = \lVert \mathbf{w} \odot \Omega_{de} \rVert_p$	-	$\Omega_{de} = (F'_d, F'_a, F'_{da}, F'_{ed}, F_{A_d})$
Uncut fibres (inside the hole):				
7	$F_{L,95\%}$ [13]	$F_{L,95\%} = \frac{L_{95\%} - L_{f,95\%}}{L_{95\%}}, \in [0, 1]$	-	$L_{95\%}$: complete circumferential length at 95% of diameter D_{nom} $[\rho]$; $L_{95\%} - L_{f,95\%}$: arc length covered by uncut fibres at 95% of diameter D_{nom} $[\rho]$
8	F_n [13]	$F_n = \tanh\left(\frac{n_{\text{uncut}}}{15}\right), \in [0, 1)$	-	n_{uncut}: number of uncut fibres
9	$F_{A_{cov}}$ [13]	$F_{A_{cov}} = 1 - \frac{A_{\text{free}}}{A_{\text{nom}}}, \in [0, 1]$	-	A_{free}: inside hole area uncovered by uncut fibres $[\rho^2]$
10	F_{free}	$F_{free} = 1 - \frac{D_{free}}{D_{nom}}, \in [0, 1]$	-	
11	F_{id}	$F_{id} = \frac{D_{\text{nom}} - 2 \times D_{\text{min}}}{D_{\text{nom}}}, \in [0, 1]$	-	D_{min}: minimum distance between the circle center and uncut fibres $[\rho]$
12	Q_u	$Q_u^{(p)} = \lVert \mathbf{w} \odot \Omega_{de} \rVert_p$	-	$\Omega_u = (F_{L,95\%}, F_n, F_{A_{cov}}, F_{free}, F_{id})$

with the p-norm is given by,

$$\mathbf{w}^{(p)} = \alpha^{(p)} / \left(\lVert \alpha^{(p)} \rVert_p \right)^{\frac{1}{p}} \tag{7}$$

The threshold $\mu = 0.05$ was selected after evaluating different choices of μ, as a balance between sensitivity to feature variation and robustness against excessive weight disparity.

The choice of median, mean, and mode for weight determination is motivated by both the characteristics of the p-norms. For the 1-norm, the median provides a robust central tendency that mitigates the influence of outliers, ensuring that it balances the different defect characteristics. For the 2-norm, the mean captures the average magnitude of factors, allowing larger defects to be emphasized and reducing sensitivity to smaller defects. For the ∞-norm, the mode represents the most frequently observed value, aligning the weighting with the worst-case assessment while discounting other smaller defects. This approach yields interpretable weights that adapt to the intended decision logic of hole quality evaluation. This allows practitioners to select the formulation that best matches the intended decision logic or risk posture of the inspection task.

B. Image Processing Algorithm for Evaluation

The proposed algorithm performs numerical pixel-level computation that exploits the high-resolution images of drilled holes where quantisation effects of boundaries become negligible. It consists of three stages, with stage 1 taking a grayscale image as input and represents it in a suitable format for analysis and visualization. Stage 2 then computes relevant parameters related to the hole quality, and finally stage 3 generates the output in the form of evaluation metrics. The implementation of the numerical computation and visualization were carried out using Python libraries - Numpy, Matplotlib, OpenCV and Pandas. The stages of the proposed algorithm (see flowchart in Figure 3) implementing the analytics are described in detail through Figure 2 with each panel within the Figure being described within the three stages:

1) Stage 1. Image Description

A. The initial input consists of a high-resolution grayscale image, captured at a resolution of 7804 × 7804 pixels using an Alicona™ µCMM (optical coordinate measuring machine[1]).

---

[1] https://www.alicona.com/en/products/optical-cmm-machine

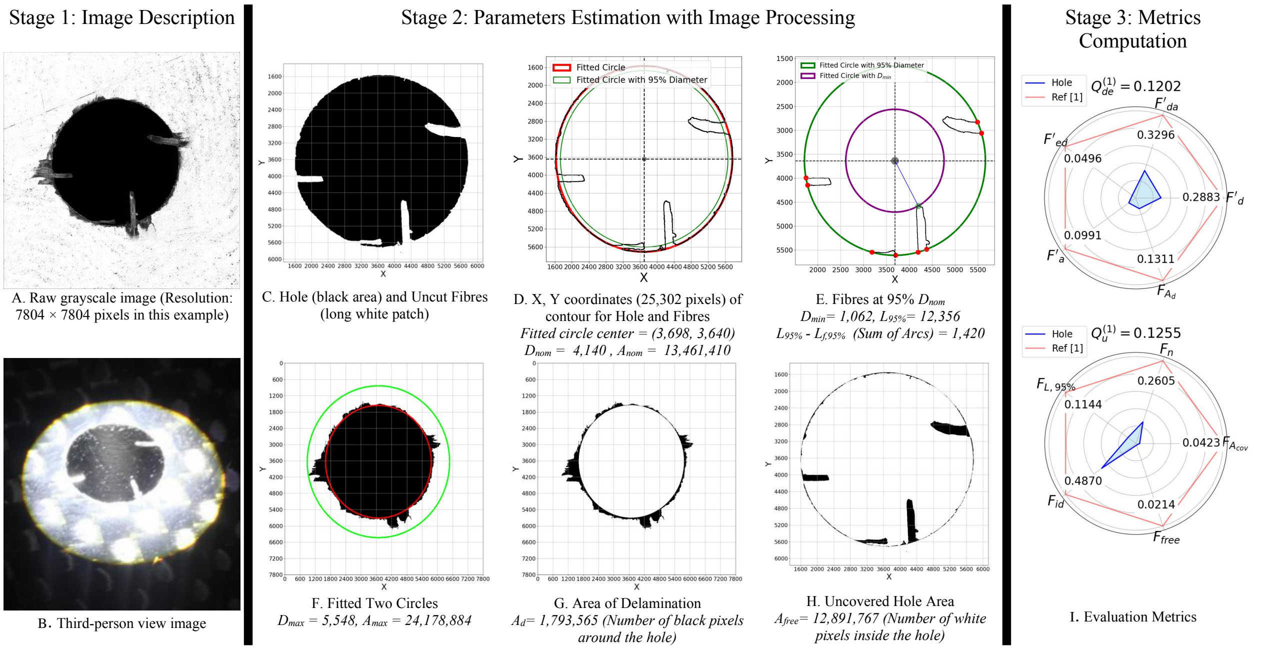

A. Raw grayscale image (Resolution: 7804 × 7804 pixels in this example)

B. Third-person view image

C. Hole (black area) and Uncut Fibres (long white patch)

D. X, Y coordinates (25,302 pixels) of contour for Hole and Fibres
Fitted circle center = (3,698, 3,640)
D_{nom} = 4,140 , A_{nom} = 13,461,410

E. Fibres at 95% D_{nom}
D_{min}= 1,062, $L_{95\%}$= 12,356
$L_{95\%}$ - $L_{f,95\%}$ (Sum of Arcs) = 1,420

F. Fitted Two Circles
D_{max} = 5,548, A_{max} = 24,178,884

G. Area of Delamination
A_d= 1,793,565 (Number of black pixels around the hole)

H. Uncovered Hole Area
A_{free}= 12,891,767 (Number of white pixels inside the hole)

I. Evaluation Metrics

Fig. 2: Results from the image processing pipeline described in section II for hole quality evaluation.

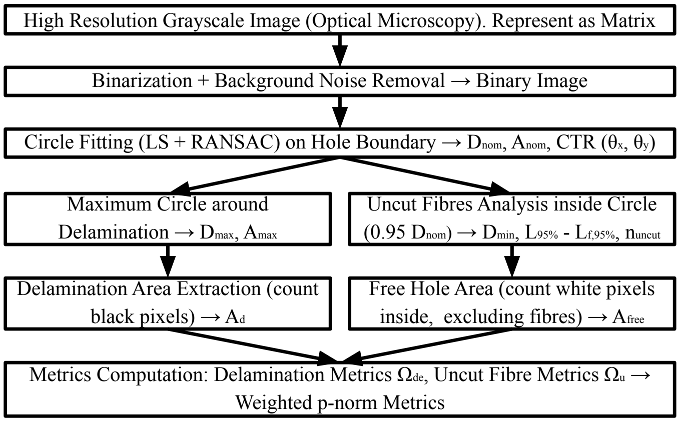

Fig. 3: Flowchart of the proposed image-processing pipeline for automated evaluation of hole quality in CFRP. LS: Least Squares. RANSAC: Random Sample Consensus. CTR: Circle Center Coordinates. See Figure 2 for the result demonstration.

The image exhibits a variety of features, including the hole, represented as a set of black pixels (I_{hole}), surrounded by uncut fibres (I_{uncut}) and delamination areas (I_{delam}), both encoded as gray-scale pixels. The CFRP stack surface is depicted by the majority of the image pixels, which are white (I_{CFRP}) and appear as background. The image can be represented as a matrix $\mathbf{I}$ where each element $I_{i,j}$ corresponds to the intensity value of the pixel at coordinates (i, j), within the domain of the image, denoted as $I \in \mathbb{R}^{7804\times7804}$.

B. An auxiliary image, captured from a third-person perspective, is used to capture additional visual information regarding the uncut fibres within the hole. It highlights uncut fibres (I_{uncut}) and provides context for their location relative to the hole.

2) *Stage 2. Parameter Estimation with Image Processing*

C. The initial step in processing the grayscale image focuses on extracting hole quality metrics associated with uncut fibres. This involves the removal of gray pixels, which possess intensity values in the range $[1, 254]$, noting that a value of 0 denotes a black pixel and 255 denotes a white pixel. This operation highlights the underlying features of the drilled hole and fibres, resulting in a binary image $\mathbf{I}_b$, where:

$$\mathbf{I}_b(i, j) = \begin{cases} 1 & \text{if } I(i, j) \in [1, 255] \\ 0 & \text{otherwise} \end{cases}$$

This image reveals the contours of both the hole and the surrounding fibres, where the black pixels correspond to the hole, and the white pixels within the region of the nominal hole correspond to the uncut fibres. This transformation isolates the relevant features for subsequent geometric analysis.

D. To compute the geometric properties of the drilled hole, the X and Y coordinates of the boundary pixels (black pixels adjacent to white pixels) are extracted and stored in the set $\mathcal{V} = \{(\mathcal{X}_0, \mathcal{Y}_0)\}$, respectively. This set represents the pixel locations that form the boundary of the drilled hole and uncut fibres, and the subsequent least squares [27] and random sample consensus (RANSAC) [28] algorithms are used to fit a circle to these coordinates. RANSAC filters out outliers (uncut fibres and irregularities), and then the circle parameters are computed from the non-outliers using algebraic least squares. The objective function for the least squares method is given by: $\min_{\theta,r} \sum_{(x_i,y_i)\in\mathcal{V}} \left(\sqrt{(x_i-\theta_x)^2+(y_i-\theta_y)^2}-r\right)^2$ where (θ_x, θ_y) is the center coordinates of the circle, and r is the radius of the circle. The solution to this minimization provides the optimal center coordinate $(\hat{\theta}_x, \hat{\theta}_y)$ and the nominal diameter $D_{nom} = 2r$, which leads to the nominal area $A_{nom} = \pi r^2$. The red circle in the processed image corresponds to the nominal hole, and the green circle, with a diameter $0.95D_{nom}$, is used to identify the region of interest for subsequent analysis of uncut fibres (as depicted in Figure 2D).

E. In the next step, the minimum distance D_{min} between the center of the nominal hole circle $(\hat{\theta}_x, \hat{\theta}_y)$ and the uncut fibres within the green circle (with diameter $0.95D_{nom}$) is computed and the hole region defined. The uncut fibres coordinates as represented with black pixels in this region are stored in the set $\mathcal{U} = \{(\mathcal{X}_u \times \mathcal{Y}_u)\}$. The minimum distance D_{min} is calculated as: $D_{min} = \min_{(x_i,y_i)\in\mathcal{U}} \sqrt{(x_i - \hat{\theta}_x)^2 + (y_i - \hat{\theta}_y)^2}$. This distance defines the proximity of the uncut fibres to the center of the hole. The total circumferential length at 95% of the nominal diameter is given by: $L_{95\%} = 0.95 \cdot \pi D_{nom}$. The length of the circumferential region covered by uncut fibres is computed as the difference: $L_{95\%} - L_{f,95\%}$ where $L_{f,95\%}$ represents the length of the circumferential arc that is blocked by the uncut fibres, It is determined by counting the number of uncut fibres that intersect the arc defined by the green circle (as shown by the red points in Figure 2E). The calculation process is as follows: Let $\mathcal{B} = \{(\mathcal{X}_b, \mathcal{Y}_b)\}$ be the set containing the X and Y coordinates of the boundary pixels of uncut fibers (black pixels adjacent to white pixels), and let $\mathcal{H}_{95\%} = \{(\mathcal{X}_h, \mathcal{Y}_h)\}$ be the set containing the X and Y coordinates of the boundary of the green circle with a 95% nominal diameter. The intersection points between the uncut fibre boundaries and the green circle are determined as $\mathcal{P} = \{(x, y) \mid (x, y) \in \mathcal{B} \cap \mathcal{H}_{95\%}\}$, where $\mathcal{P}$ represents the set of crosspoints, which are marked in red and stored for further calculations. Given red intersection points (x_i, y_i) on a circle with center (x_c, y_c) and radius r, the angle corresponding to each point is computed as $\theta_i = \arctan 2(y_i - y_c, x_i - x_c)$. The arc length between two red points (x_i, y_i) and (x_{i+1}, y_{i+1}) is given by $L_i = 2\pi r \times \frac{|\theta_{i+1} - \theta_i|}{2\pi} = r|\theta_{i+1} - \theta_i|$, where $|\theta_{i+1} - \theta_i|$ is the absolute angular difference between them in radians. The total arc length is computed as the sum $L = \sum L_i$. The number of uncut fibers, n_{uncut}, is given by $n_{uncut} = \frac{|\mathcal{P}|}{2}$, since each uncut fiber contributes exactly two crosspoints on the circular boundary.

F. The image background removal technique is applied to isolate the uncut fibre area within the hole region. A connectivity-based algorithm identifies all the pixels related to the fibres, and the maximum circle D_{max} that encompasses all these pixels is determined. The center of D_{max} coincides with the center of the nominal hole, and the area of the maximum circle is denoted as A_{max}, computed as: $A_{max} = \frac{1}{4}\pi D_{max}^2$. This circle is shown in Figure 2F as the green circle, while the red circle represents the nominal hole circle D_{nom}.

G. The next step involves isolating the delamination area from the image obtained from step **A**. To achieve this, the regions within the nominal circle D_{nom} and the maximum circle D_{max}, estimated in step **D**, are removed. This results in the black pixels being those related to delamination regions. The delamination area (i.e., A_d), is then computed by counting the number of black pixels remaining in the image. This area is given by: $A_d = \sum_{(i,j)\in\mathcal{I}_d} \mathbf{I}_b(i, j)$ where $\mathcal{I}_d$ represents the set of pixel indices within the delamination region.

H. Finally, the area of the hole that is not covered by fibres, denoted as A_{free}, is computed by counting the number of white pixels inside the nominal circle D_{nom} that are not part of the uncut fibres. This uncovered area is calculated as: $A_{free} = \sum_{(i,j)\in\mathcal{I}_{free}} \mathbf{I}_b(i, j)$ where $\mathcal{I}_{free}$ represents the set of pixel indices corresponding to the uncovered area inside the nominal circle. This area is depicted in Figure 2H.

TABLE II: Runtime and memory requirements of the processing pipeline on images of increasing resolution. Bold text shows the original image resolution captured by optical microscopy.

Image resolution	Megapixels	Processing time [s]	Peak RAM (MB)
582 × 582	0.3	0.29	3
1165 × 1165	1.4	1.2	11
2331 × 2331	5.4	5	46
4662 × 4662	21.7	19	166
9324 × 9324	**86.9**	**82**	**705**
13986 × 13986	195.6	186	1140
18648 × 18648	347.7	332	1595

3) Stage 3. Metrics Computation

I. The metrics for evaluating delamination damage and uncut fibres are computed using the formulae given in Table I. The p-norm with $p = 1$ was used in Figure 2 radar charts for visualization. In practice, other values of p would also be used. The upper radar chart displays metrics related to delamination, while the lower radar chart shows metrics concerning uncut fibres. All metrics are scaled to the range $[0, 1]$ as indicated in Table I, where lower values correspond to better performance. Reference values for each metric are also included, where "reference" denotes the values corresponding to the upper limits of delamination and uncut fibres, respectively.

C. Computational Performance and Scalability

Although the proposed framework is applied offline in the post-processing stage of robotic drilling and is therefore not subject to real-time constraints, we evaluated its computational requirements to facilitate practical deployment. Measurements were performed on an AMD Ryzen 7 7700X CPU. Table II reports the processing time and peak memory consumption of the pipeline for square images of increasing resolution derived from our industrial 9324 × 9324 pixel (86.9 Mpixel) dataset. Higher-resolution images were generated using Lanczos resampling [29], whereas lower-resolution images were obtained via area-averaging [30]. The algorithm exhibits near-linear scaling with the number of pixels. On production-resolution images of 9324 × 9324 pixels (approximately 87 million pixels), the entire pipeline completes in approximately 80 seconds while consuming around 700 MB of RAM. These performances are suggestive of their suitability for supporting identification of image/vision system requirements and limitations for offline vs. inline systems, based on process runtime requirements.

III. EXPERIMENTS AND RESULTS

A. Robotic Drilling Platform and Hole Properties

The purpose of the drilling trials was to feed into a large dataset of drilling process factors, hole quality responses,

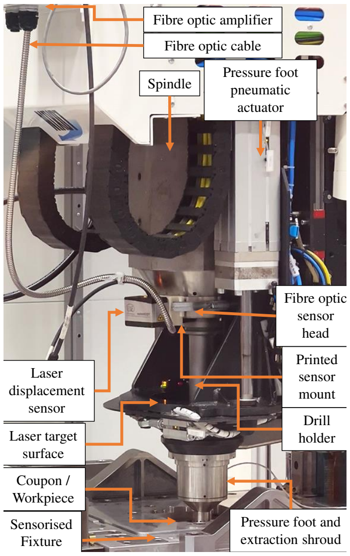

(a) Drilling platform and fixture.

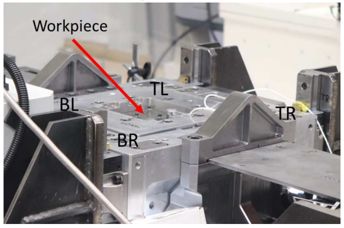

(b) Example workpiece mounted in the fixture.

Fig. 4: Equipment set-up of the machining platform.

and in-process signals. This derives from the knowledge that mechanical performance of structures is affected by the hole quality measures, which in turn are influenced by the drilling process factors [21]. In this paper, data from these trials is being used to develop and test methods for delamination and uncut fibre assessment and some analysis to relate drilling parameters to metrics. The robotic drilling platform utilizes a Loxin "Tricept", a five-axis parallel kinematic machine and is illustrated in Figure 4a. This system is equipped with a custom end effector that features a pressure foot and a spindle mounted on a quill axis. The workpiece is securely held by a precision clamping system, which is fixed to a robust metallic base, as shown in Figure 4b. The alignment points which serve as reference markers for proper orientation are labeled TR, TL, BR, and BL, corresponding to the top-right, top-left, bottom-right, and bottom-left corners of the workpiece, respectively.

The workpieces utilized in the study consist of a layered stack of Titanium (Ti) and Carbon Fiber Reinforced Polymer (CFRP), with Ti as the top layer and CFRP as the bottom layer. A thin interlayer gap representative of assembled stack components, filled with wet replica sealant, separates the two materials. The primary focus of the assessment was the defects at the CFRP hole exit part. The test involved two workpieces, labeled "105" and "106" on which 24 holes were drilled across the stacks, with workpiece "105" has 10 holes, while workpiece "106" has 14 holes. The manufacturing process conditions for the drilling operation were used varying feed rates and spindle speeds, as detailed in Table III. Additionally, different drills were also employed for the holes, introducing some variability in the drilling process.

TABLE III: Drilling parameter and properties for workpieces 105 and 106.

Attributes	Group 1	Group 2	Group 3
Hole index	**106**: C1	**105**: A1, A2, A3, A4, B1, B2, B3, B4, C1, C2; **106**: C2, C3, C4, D3, D4	**106**: A1, A2, A3, A4, B1, B2, B3, B4
Feed rate [mm/min]	214	345	600
Spindle speed [Rev/min]	3568	5764	6000
Number of holes with uncut fibres	0	5	7
Number of holes	1	15	8
Percentage of holes with uncut fibres	0%	33.3%	87.5%

B. Experimental Results

The application of the image processing algorithm and the resulting computed metrics on the two work pieces and selected holes are shown in Figure 5. The Figure shows grayscale images of hole exits as well as their corresponding radar charts of the quality parameters for delamination and uncut fibre defects. The images displayed in Figure 5 ($106_{C1}, 105_{B2}, 105_{B3}, 106_{D3}, 106_{A4}$) show a progressive deterioration in hole exit quality. This decline is characterized by an increasing presence of uncut fibres and to a larger extent of delamination damage.

Uncut fibres are not seen in the images of holes 106_{C1} and 105_{B2} and hence only the radar charts for delamination are presented. The delamination is characterized by two small, distinct patches located in the upper right and lower left regions for the hole 106_{C1}. In contrast, hole 105_{B2} exhibits two slightly larger delamination patches positioned on the top and bottom of the hole. The Q_{de} computed for these two holes shows their sensitivity to low levels of delamination noting that the value for 106_{C1} (0.0327) is lower than that of 105_{B2} (0.0645). Similarly, a comparison of the delamination defects of the hole 105_{B3} and 106_{A4} shows that for the former, delamination manifests as several small patches located at the top of hole, while for the latter, a large patch on the left side and additional thin branches extending around the hole. The delamination for the hole 106_{D3} is somewhat more pronounced, with three distinct delamination patches encircling the hole are observed. The Q_{de} values computed for these three holes are 0.0870 (105_{B3}), 0.1102 (106_{A4}), and 0.1199 (106_{D3}) and are relatively consistent with the expectations of the delamination quality measure. Figure 5B presents the delamination metrics Q_{de} for five different holes, revealing a clear trend: as the visible extent of delamination damage increases, the corresponding Q_{de} values also rise, underscoring the sensitivity of the metric to variations in delamination severity.

Analysis of the uncut fibre defects for the five holes considered are also analysed. As seen in the BW Image in Figure 5,

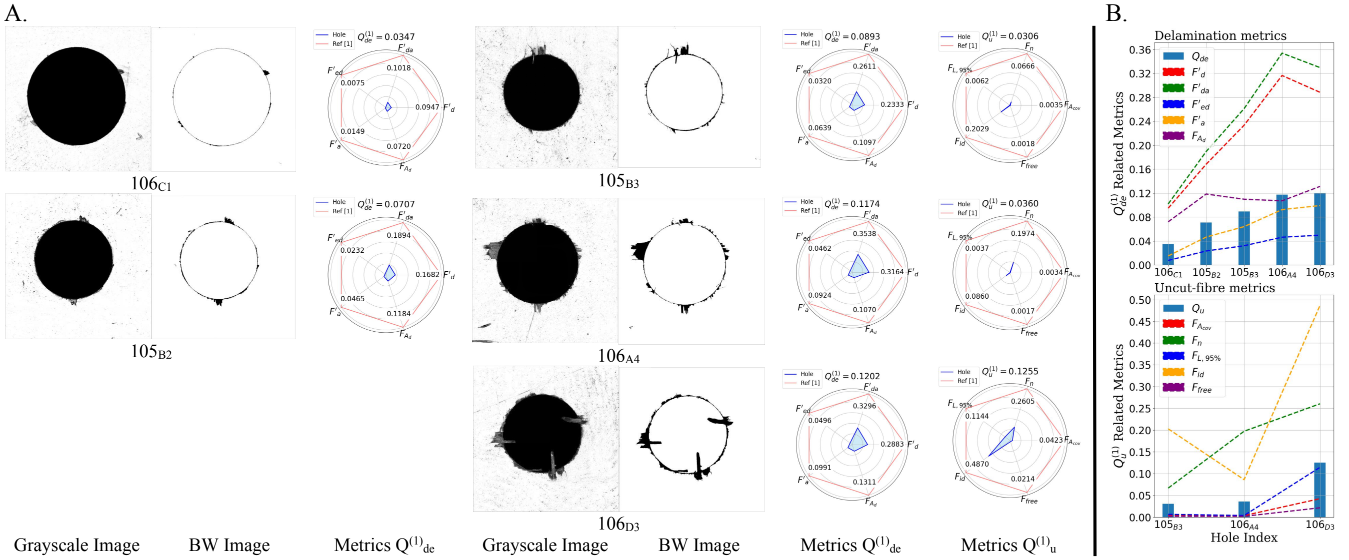

Fig. 5: **A.** Images and radar charts depicting hole exit quality. Alicona µCMM imaging system was used to obtain grayscale images. Image processing framework was used to remove background and noise to obtain the black-and-white (BW) images, that serve to highlight the delamination and uncut fibres. Radar charts for metrics $Q_{de}^{(1)}$ and $Q_{u}^{(1)}$ represent delamination and uncut fibres respectively. The reference values for $Q_{de}^{(1)}$ and $Q_{u}^{(1)}$ are set to 1. **B.** Bar and line charts for delamination metrics and Uncut-fibre metrics.

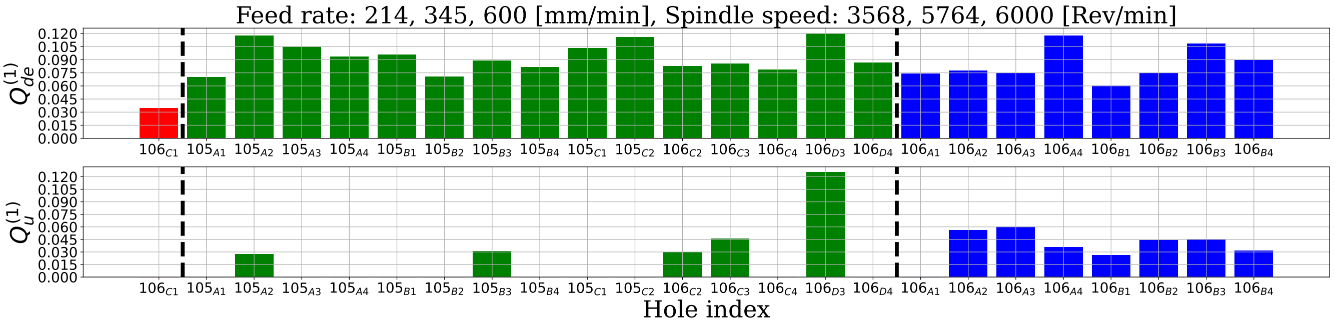

Fig. 6: Combined metrics $Q_{de}^{(1)}$ and $Q_{u}^{(1)}$ for all test images. The 24 holes are categorized into three groups based on machining parameters—feed rate and spindle speed, as shown in Table III. Bar charts display the uniform metrics Q_{de} and Q_u for hole quality, divided into three categories by two bold black dashed lines. The red, green and blue bars represent holes drilled at a feed rate of 214 mm/min and spindle speed of 3568 Rev/min, holes drilled at a feed rate of 345 mm/min and spindle speed of 5764 Rev/min, and holes drilled at a feed rate of 600 mm/min and spindle speed of 6000 Rev/min respectively.

a single slender uncut fibre is positioned towards the top of the hole in hole 105_{B3}, while two short uncut fibres are seen in hole 106_{A4}. In hole 106_{D3}, however, four long fibres and some shorter fibres are clearly visible inside the hole. The computed uncut-fibre metrics (Q_u) for these three holes are presented in Figure 5B. The measure Q_u for the hole 106_{D3}, where the presence of uncut fibres is significantly more pronounced, is computed to be approximately three times greater than those for the holes 105_{B3} and 106_{A4}, which have smaller areas associated with uncut fibres.

The complete set of results from the analysis of all test images of the drilled holes were evaluated using the combined metrics Q_{de} and Q_u, and shown in Figure 6 ($p = 1$) and Table IV ($p = 1, 2, \infty$). The metric Q_u effectively differentiates uncut fibres across various holes, irrespective of their size, provided the fibres fall within a circular area with a diameter corresponding to 95% of D_{nom}, as specified for evaluation. Fibres outside this circle are excluded from further analysis, as demonstrated in Figure 2E. Notably, Q_u also excels at distinguishing larger size uncut fibres (such as those in 106_{D3}) from smaller ones. Similarly, Q_{de} proves its ability to differentiate holes based on the extent of delamination damage, enabling a nuanced assessment of delamination severity.

To more effectively differentiate hole quality using p-norm metrics, we employ the Pareto front to quantify the number of instances that each hole dominates. For example in the hole 106_{C1}, since both its $Q_{de}^{(1)}$ and $Q_{u}^{(1)}$ (See Table IV) values are lower than those of other 23 holes, it dominates 23 other holes. Therefore, the Pareto front statistic for 106_{C1} is 23. A higher value indicates a better quality of the hole. Table V shows the statistics of 24 holes using p-norm metrics. Additionally, to further analyze the impact of machining parameters—such as spindle speed and feed rate—on hole quality, we categorized 24 holes into three groups and computed the mean Pareto front statistics for each group. The results indicate that higher machining parameters are associated with worse hole quality.

Using different p-norms (1, 2 and ∞) allows us to capture diverse aspects of the defect features, such as if there is a single

TABLE IV: p-norm ($p = 1, 2, \infty$) metrics Q_{de} and Q_u for all 24 test images.

Holes	$Q_{de}^{(1)}$	$Q_{de}^{(2)}$	$Q_{de}^{(\infty)}$	$Q_u^{(1)}$	$Q_u^{(2)}$	$Q_u^{(\infty)}$
105_{A1}	0.0703	0.0743	0.0622	0	0	0
105_{A2}	0.1174	0.1049	0.0953	0.0272	0.0274	0.0666
105_{A3}	0.1048	0.0905	0.0838	0	0	0
105_{A4}	0.0938	0.0809	0.0709	0	0	0
105_{B1}	0.0960	0.0947	0.0758	0	0	0
105_{B2}	0.0707	0.0615	0.0465	0	0	0
105_{B3}	0.0893	0.0782	0.0639	0.0306	0.0362	0.0676
105_{B4}	0.0815	0.0707	0.0570	0	0	0
105_{C1}	0.1033	0.0897	0.0804	0	0	0
105_{C2}	0.1162	0.1004	0.0972	0	0	0
106_{A1}	0.0741	0.0708	0.0558	0	0	0
106_{A2}	0.0777	0.0685	0.0515	0.0558	0.0563	0.1974
106_{A3}	0.0749	0.0695	0.0663	0.0604	0.0604	0.1974
106_{A4}	0.1174	0.1046	0.0924	0.0360	0.0456	0.1974
106_{B1}	0.0606	0.0544	0.0474	0.0261	0.0265	0.0666
106_{B2}	0.0752	0.0656	0.0502	0.0443	0.0433	0.1325
106_{B3}	0.1082	0.0961	0.0825	0.0444	0.0449	0.1325
106_{B4}	0.0904	0.0829	0.0763	0.0315	0.0314	0.0666
106_{C1}	0.0347	0.0317	0.0240	0	0	0
106_{C2}	0.0825	0.0787	0.0783	0.0298	0.0339	0.0666
106_{C3}	0.0856	0.0747	0.0605	0.0459	0.0498	0.0757
106_{C4}	0.0785	0.0708	0.0630	0	0	0
106_{D3}	0.1202	0.1052	0.0991	0.1255	0.1194	0.2605
106_{D4}	0.0868	0.0765	0.0606	0	0	0

TABLE V: Pareto front statistics for 24 holes. Columns "$p = 1$", "$p = 2$", and "$p = \infty$" show how many instances each hole dominates based on metrics in Table IV. Figure 7 visualizes these statistics. Red, green, and blue represent distinct machining parameter sets (Figure 6). Each "Mean" column gives the average for the respective colour group.

Holes	$p = 1$	Mean	$p = 2$	Mean	$p = \infty$	Mean
106_{C1}	23	23.0	23	23.0	23	23.0
105_{A1}	21	8.1	14	7.8	14	8.3
105_{A2}	1		1		1	
105_{A3}	5		6		4	
105_{A4}	8		9		10	
105_{B1}	7		5		9	
105_{B2}	20		21		22	
105_{B3}	4		3		4	
105_{B4}	14		17		17	
105_{C1}	6		7		6	
105_{C2}	3		3		1	
106_{C2}	6		3		4	
106_{C3}	1		1		4	
106_{C4}	15		15		13	
106_{D3}	0		0		0	
106_{D4}	11		12		15	
106_{A1}	19	5.1	16	5.3	18	5.9
106_{A2}	1		2		3	
106_{A3}	1		1		2	
106_{A4}	1		1		1	
106_{B1}	11		11		11	
106_{B2}	4		6		5	
106_{B3}	1		2		2	
106_{B4}	3		3		5	

large defect or defects uniformly found in all regions. For the former, the $p = \infty$ norm will be high and $p = 1$ norm will be low whereas for the latter, the $p = \infty$ norm will be lower and the $p = 1$ norm will be higher. The results for each p-norm across holes illustrate these characteristics well and also seen in terms of the Pareto dominance counts based ranking. For instance in Table V, hole 106_{C1} consistently dominates with counts of 23 (out of 24) across all norms, indicating strong overall high quality with only low-magnitude defects, suggesting it would pass any quality inspection. On the other end, hole 106_{D3} has zero dominance counts for all norms reflecting high defect levels, which emphasizes the poor hole quality across all quality metrics.

Another example, hole 106_{A1} has a higher 1-norm dominance count (19) compared to its 2-norm and ∞-norm dominance counts (16 and 18), indicating balanced defect levels without excelling in high-value defect metrics. This demonstrates the 1-norm's usefulness in providing a general aggregation of the metrics, preventing any single metric with high value from dominating the final quality measure. In contrast, hole 105_{B4} has a dominance count of 14 for the 1-norm and, 17 for the 2- and ∞- norms. This is reflective of the fact that some or a small set of the quality metrics having large values associated with defects with other metrics being small. The 1-norm, 2-norm and ∞-norm thus offer different perspectives of the hole defects as described by the quality metrics: the 1-norm captures overall balanced performance across all metrics; the 2-norm emphasizes higher-magnitude defects but tries to also give importance to all metrics; and the ∞-norm focuses solely on the largest defect metric, highlighting worst-case scenarios. This adaptable approach allows for tailored defect assessments aligned with specific evaluation goals, ensuring a thorough analysis across all possible cases.

Additionally, based on visual assessments of hole quality, we propose establishing thresholds along with specific functions to categorize holes into several groups (see Figure 7). As shown in Figure 7B, the dotted red line defined by the function $\sqrt{0.12 \cdot (Q_{de})^2 + 0.03 \cdot (Q_u)^2} = 0.06$, while the green solid line defined by the function $\sqrt{0.12 \cdot (Q_{de})^2 + 0.12 \cdot (Q_u)^2} = 0.12$, effectively segmenting all 24 data points into three groups and distinguishing between high, moderate and low-quality holes. The hole quality categorized by the proposed functions and thresholds closely aligns with visual judgment, offering a new alternative automated image processing based method for evaluating hole quality.

The influence of machining parameters on delamination was also investigated. The findings suggest that higher spindle speeds lead to increased values of Q_{de}, indicating a greater impact on delamination (See Figure 8). We also examined the effect of machining parameters on uncut fibres and found that higher feed rates are potentially associated with an increased number of holes containing uncut fibres and a higher Q_u value, except for hole 106_{C1} (See Figure 9).

The combined metrics were analyzed in relation to the machining parameters for potential correlations. Preliminary observations suggest that higher values of machining parameters, such as feed rate and spindle speed, may contribute to an increased occurrence of holes with uncut fibres (evidenced by higher Q_u values), as inferred from Table III and Figure 6. However, no similar trend was observed for Q_{de}, with the exception of the lowest parameter setting. It is important to note that factors such as vibration and tool wear, both of which are known to impact hole quality, were present during the drilling trials and the inclusion of these with the image data for analysis can lead to improved quality assessment. Furthermore, these trials were not specifically designed to establish direct correlations between machining parameters and delamination, and therefore, drawing definitive conclu-

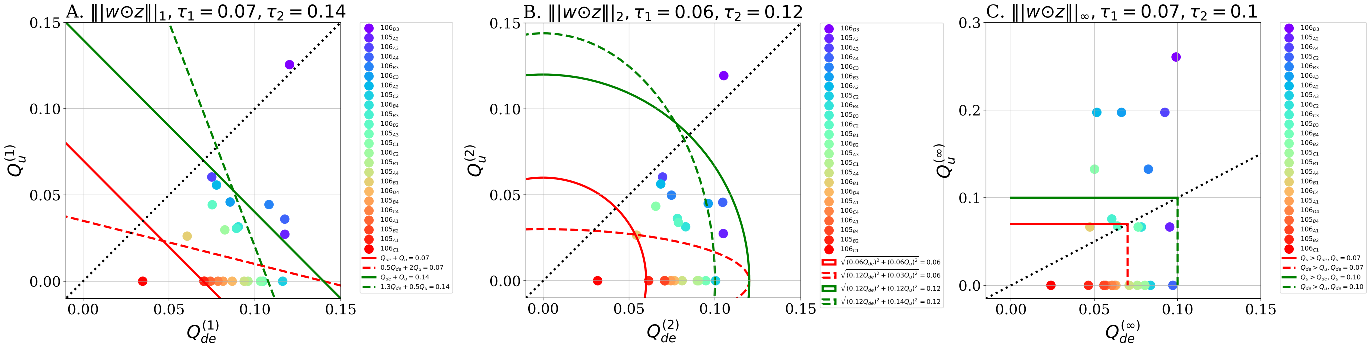

Fig. 7: The p-norm ($p = 1, 2, \infty$) metrics for Q_{de} and Q_u are classified using the boundary equation $||w_Q \odot Q||_p = c$, where $Q = [Q_{de}, Q_u]$ and w_Q is the weight. The weight-boundary pairs can be expressed as $([w^{(p)}_{Q_{de}}, w^{(p)}_{Q_u}], c^{(p)})$. For $p = 1$ with thresholds $\tau_1 = 0.07$ and $\tau_2 = 0.14$, classification uses four weight-boundary pairs: $([1, 1], 0.07)$, $([0.5, 2], 0.07)$, $([1, 1], 0.14)$, and $([1.3, 0.5], 0.14)$. For $p = 2$ with $\tau_1 = 0.06$ and $\tau_2 = 0.12$, classification applies $([0.06, 0.06], 0.06)$, $([0.12, 0.03], 0.06)$, $([0.12, 0.12], 0.12)$, and $([0.12, 0.14], 0.12)$. For $p = \infty$ with $\tau_1 = 0.07$ and $\tau_2 = 0.10$, classification includes $([0, 1], 0.07)$, $([1, 0], 0.07)$, $([0, 1], 0.10)$, and $([1, 0], 0.10)$, segmenting 24 metrics. The black dashed line $Q_{de} = Q_u$ serves as a reference for data trends, with points colored by Pareto front dominance.

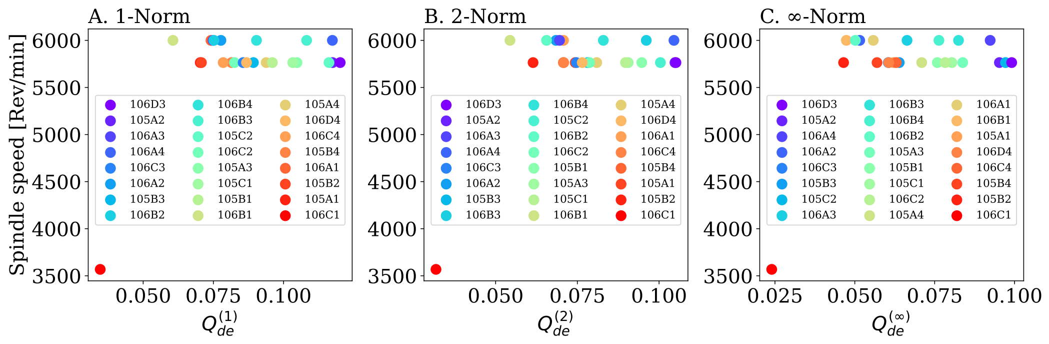

Fig. 8: p-norm metrics for Q_{de} and spindle speed. The figure shows the relationship between p-norm Q_{de} metrics and spindle speed. Scatters are colour-mapped by the number of dominated instances from Pareto front statistics.

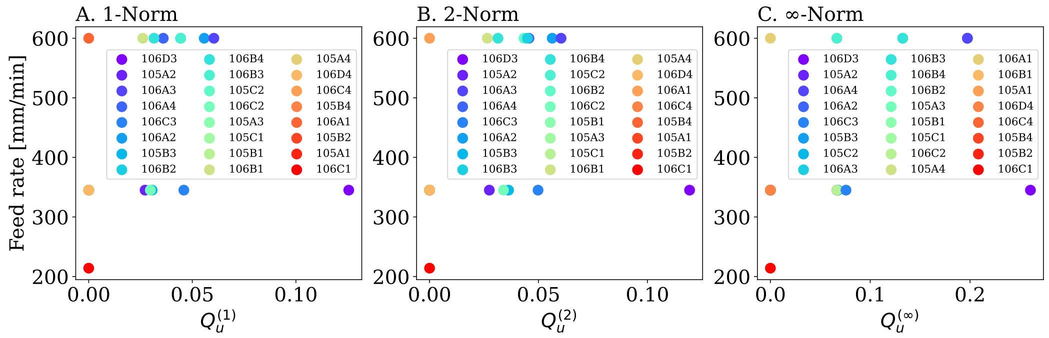

Fig. 9: p-norm metrics for Q_u and feed rate. The figure shows the relationship between p-norm Q_u metrics and feed rate. Scatters are colour-mapped by the number of dominated instances from Pareto front statistics.

sions about causal relationships based on this limited dataset is not recommended. The framework presented has real-world application for automated quantification of delamination and uncut fibres, incorporating various individual metrics.

IV. DISCUSSION

The scientific contribution of this work lies in establishing a unified image-processing framework that integrates multiple defect metrics through a principled multi-criteria formulation, rather than relying on a single metric as commonly adopted in existing studies. While prior works typically focus on one defect factor, the proposed approach recognises that different metrics capture complementary physical characteristics of drilling-induced defects. By combining these metrics using weighted p-norm aggregation and analysing their trade-offs via Pareto-front exploration, the framework provides a more holistic and robust assessment of hole quality.

The experimental dataset in this study analyses 24 drilled holes that appear limited at first instance. However, collection of robust datasets is currently a major challenge for stack machining applications. This study was a feasibility study to demonstrate an analysis pipeline with a view to further validation and testing on larger datasets in the future. The key issues with any limited dataset are the coverage of potential defects and their sensitivity to detection and quantification. The defect coverage was induced through the variation of the drilling process parameters. The robust combined metric for defect quantification and the Pareto front analyses have shown promise, although their generalizability demands that large datasets be used across multiple production batches, varying process conditions, and different material types. Comprehensive comparative studies with established techniques such as 3D microscopy, ultrasonic C-scan, and expert manual evaluations need to be conducted to benchmark accuracy, repeatability, and efficiency, as well as to establish quantitative correlations with mechanical performance.

The proposed framework, although initially developed and benchmarked using a dataset, is fully designed for deployment in real manufacturing environments. It operates on inputs that are routinely obtainable in industrial drilling processes, i.e., end-face images, and its algorithms are independent of dataset-specific characteristics. The modular structure of the framework enables seamless integration with inline machine vision systems, allowing direct inference without additional specialized hardware. These features ensure that the methodology is readily transferable to real-world robotic drilling operations, supporting practical applicability beyond controlled experimental conditions. While it has generic applicability, instances where optical microscopy instrumentation cannot be placed within the manufacturing setup may limit its universality.

The use of optical microscopy in this study reflects the constraints of the available dataset rather than a requirement of the proposed framework, which does not depend on microscopic resolution. The defect metrics extracted are derived from 2D geometric information that can be obtained using standard industrial vision systems, such as end-effector-mounted cameras integrated into bespoke aerospace drilling and assembly platforms. Consequently, the framework is well positioned for translation to a shop-floor environment, where it can also be used to determine minimum image-quality requirements (e.g. minimum x resolution at y size) to guide the specification of practical in-line inspection hardware.

The accuracy and metrological traceability of image-based assessment in composite drilling critically depend on the calibration and performance of the imaging system. Pixel-scale calibration must be rigorously validated to ensure that defect metrics, such as delamination and uncut-fibre dimensions, accurately reflect physical measurements. Achieving reliable and repeatable measurements requires industrial-grade imaging systems combined with consistent acquisition protocols and validation against certified reference standards. By providing quantitative, image-derived metrics, the proposed framework enables systematic defect evaluation while also supporting the development of standardized vision-based inspection procedures. When integrated with established metrological guidelines and documentation of calibration and uncertainty, such a framework has the potential to contribute to future standardization efforts for composite drilling quality assessment.

The proposed ranking framework provides a systematic and efficient approach for assessing hole quality by integrating multiple defect metrics, such as delamination size, uncut-fibre area, and defect length, into a single aggregated score. The use of p-norm aggregation emphasizes the most severe defects, allowing rapid identification of holes that are likely to have the greatest impact on structural performance. While the framework produces relative rankings rather than absolute quality thresholds, it offers practical utility for process evaluation and comparative studies, enabling early identification of critical defects and guiding process optimization. Furthermore, by correlating aggregated defect scores with structural performance metrics, such as residual strength or fatigue life, the framework has potential to be a foundation for establishing preliminary acceptance guidelines and informing the development of application-specific quality criteria. This integrated approach bridges experimental observations and engineering requirements, facilitating more informed decision-making in defect assessment and quality control.

The proposed framework demonstrates strong potential for practical, on-site deployment in industrial composite drilling by enabling quantitative, image-based assessment of hole quality. It is compatible with machine-mounted vision systems, such as cameras integrated with robotic end effectors, which could capture images in-process or immediately post-process to support rapid defect evaluation. Although the current study focuses on controlled, post-process measurements, prior work [31] has shown that correlations between visualized defect metrics and in-process sensing signals, such as acoustic emissions, can facilitate the development of predictive models for real-time hole quality estimation. Effective integration with manufacturing execution systems and shop-floor workflows would require further development, including synchronization with robotic operations, standardized imaging protocols, and real-time data processing.

Despite the encouraging results, several limitations of the present work should be acknowledged. (i) The experimental validation is based on a limited number of drilled holes from a single dataset, which constrains statistical generalisation across different materials, tooling configurations, and production batches. (ii) The proposed framework provides relative defect rankings rather than absolute acceptance thresholds, as direct correlations with mechanical performance (e.g., residual strength or fatigue life) were not established. (iii) The current analysis is performed on post-process images acquired under controlled conditions, whereas in-process or inline deployment introduces challenges related to imaging variability, calibration stability, and real-time computation.

V. CONCLUSION

This study addresses challenges in the quantitative assessment of drilling-induced defects in metal-CFRP composite materials and proposes a novel evaluation and decision-making framework. To cope with defect types of fundamentally different morphology and physical mechanisms, such as delamination and uncut fibres, a multi-metric synchronous extraction framework and a weighted p-norm fusion strategy are developed. These enable diverse defect descriptors to be integrated into a single, configurable quantitative quality measure. Then, by introducing multi-objective decision-making concepts, a systematic evaluation framework based on Pareto-front analysis and explicit quality-level partitioning is established. This allows objective ranking and grading of hole quality across batch samples. Also, it reveals the relationships between defect severity and machining parameters to support process understanding and optimisation. The specific contributions of this paper are as follows: (i) Different image-derived metrics were introduced to quantify delamination and uncut fibre defects, extending established defect factors through a high-resolution, pixel-based image-processing pipeline. (ii) A set of combined defect metrics was developed using p-norm aggregation to integrate ten complementary length- and area-based damage factors for holistic defect assessment. (iii) A multi-objective Pareto-ranking approach was proposed to evaluate relative hole quality within a population of drilled holes and to analyse trade-offs between competing defect metrics in relation to machining parameters. (iv) The feasibility and effectiveness of the proposed framework were demonstrated using a retrospective robotic metal-CFRP composite drilling dataset, supporting automated and data-driven quality assessment in high-value manufacturing.

Weighted aggregated scores using p-norms ($p = 1, 2, \infty$) were proposed towards enhancing comparability across different defect types. The use of different norm-based measure allows the different hole quality factors to be combined into a summary quality measure while giving different degrees of emphasis on the defect characteristics that may be captured by the factors. The Pareto-front analysis ranks the quality of drilled holes by quantifying dominance counts, providing a robust, multi-criteria based evaluation. Additionally, association between spindle speed, feed rate, and the defect metrics were analysed, providing further information on process parameters' impact on drilled hole quality. This novel framework allows the integration of multi-dimensional defect factors whose application can extend beyond the analysis of delamination and uncut fibre defects to other features and defects.

Future work to overcome the current limitations of this study will focus on carrying out large scale multi-batch drilling operations from which to assess robustness and repeatability of the methodologies. Integrating mechanical testing to derive performance-linked quality criteria would further validate the proposed approaches. Finally, exploring the existence of a relationship between in-process sensor signals [32], [33] and the quality of drilled holes as measured by the proposed hole quality metrics can offer optimised drilling operation with reduced defects.

Further work to advance the methods will explore the use of different weightings that can be determined from a more detailed set of experiments to identify the sensitivities of the individual factors used. These could be combined in a Bayesian setting with a priori choice of weights chosen from the individual factor and the structural analysis based on defect geometry. Use of 3D scan data instead of the 2D images which may not fully capture lifting type delamination could be investigated. Additionally, use of thermography [34], a technique for in-process detection of subsurface defects such as internal delamination and microcracks that also reveal hidden structural issues in multi-composite materials can be used that are not limited to surface inspection at post-processing stage like optical methods. This post-processing has shown success in detecting defects in CFRP [35], which could also be explored in future work.

REFERENCES

[1] D. Che, I. Saxena, P. Han, P. Guo, and K. F. Ehmann, "Machining of carbon fiber reinforced plastics/polymers: a literature review," *Journal of Manufacturing Science and Engineering*, vol. 136, no. 3, p. 034001, 2014.

[2] K. Jayakrishna, V. R. Kar, M. T. Sultan, and M. Rajesh, "Materials selection for aerospace components," in *Sustainable composites for aerospace applications*. Elsevier, 2018, pp. 1–18.

[3] N. Geier, G. Póka, and T. Szalay, "Direct monitoring of hole damage in carbon fibre-reinforced polymer (CFRP) composites," in *IOP Conference Series: Materials Science and Engineering*, vol. 448, no. 1. IOP Publishing, 2018, p. 012003.

[4] A. Haeger, G. Schoen, F. Lissek, D. Meinhard, M. Kaufeld, G. Schneider, S. Schuhmacher, and V. Knoblauch, "Non-destructive detection of drilling-induced delamination in CFRP and its effect on mechanical properties," *Procedia Engineering*, vol. 149, pp. 130–142, 2016.

[5] M. Leco, T. McLeay, and V. Kadirkamanathan, "A two-step machining and active learning approach for right-first-time robotic countersinking through in-process error compensation and prediction of depth of cuts," *Robotics and Computer-Integrated Manufacturing*, vol. 77, p. 102345, 2022.

[6] M. Leco and V. Kadirkamanathan, "A perturbation signal based data-driven gaussian process regression model for in-process part quality prediction in robotic countersinking operations," *Robotics and Computer-Integrated Manufacturing*, vol. 71, p. 102105, 2021.

[7] W.-C. Chen, "Some experimental investigations in the drilling of carbon fiber-reinforced plastic (CFRP) composite laminates," *International Journal of Machine Tools and Manufacture*, vol. 37, no. 8, pp. 1097–1108, 1997.

[8] A. Faraz, D. Biermann, and K. Weinert, "Cutting edge rounding: An innovative tool wear criterion in drilling CFRP composite laminates," *International Journal of Machine Tools and Manufacture*, vol. 49, no. 15, pp. 1185–1196, 2009.

[9] J. P. Davim, J. C. Rubio, and A. Abrao, "A novel approach based on digital image analysis to evaluate the delamination factor after drilling composite laminates," *Composites Science and Technology*, vol. 67, no. 9, pp. 1939–1945, 2007.

[10] C. Tsao, K. Kuo, and I. Hsu, "Evaluation of a novel approach to a delamination factor after drilling composite laminates using a core–saw drill," *The International Journal of Advanced Manufacturing Technology*, vol. 59, pp. 617–622, 2012.

[11] N. Geier, J. P. Davim, and T. Szalay, "Advanced cutting tools and technologies for drilling carbon fibre reinforced polymer (CFRP) composites: A review," *Composites Part A: Applied Science and Manufacturing*, vol. 125, p. 105552, 2019.

[12] N. Geier, G. Póka, and C. Pereszlai, "Monitoring of orbital drilling process in CFRP based on digital image processing of characteristics of uncut fibres," *Procedia CIRP*, vol. 85, pp. 165–170, 2019.

[13] R. Voß, M. Henerichs, S. Rupp, F. Kuster, and K. Wegener, "Evaluation of bore exit quality for fibre reinforced plastics including delamination and uncut fibres," *CIRP Journal of Manufacturing Science and Technology*, vol. 12, pp. 56–66, 2016.

[14] F. Xu, L. Sun, L. Zhu, S. Yang, D. Hui, and Y. Qiu, "X-ray 3d microscopy analysis of fracture mechanisms for 3d orthogonal woven e-glass/epoxy composites with drilled and moulded-in holes," *Composites Part B: Engineering*, vol. 133, pp. 193–202, 2018.

[15] S. Arul, L. Vijayaraghavan, S. Malhotra, and R. Krishnamurthy, "The effect of vibratory drilling on hole quality in polymeric composites," *International Journal of Machine Tools and Manufacture*, vol. 46, no. 3-4, pp. 252–259, 2006.

[16] C. Li, Y. Lei, Z. You, L. Guo, E. Zio, and H. Gao, "Vision-based defect measurement of drilled CFRP composites using double-light imaging," *IEEE Transactions on Instrumentation and Measurement*, vol. 72, pp. 1–9, 2023.

[17] F. Sun, M. Fan, B. Cao, B. Ye, and L. Liu, "High-resolution terahertz imaging of de-bonding defects in thermal barrier coatings using an optimal wavelet transform," *IEEE Transactions on Instrumentation and Measurement*, 2023.

[18] A. Caggiano, R. Angelone, and R. Teti, “Image analysis for CFRP drilled hole quality assessment,” *Procedia CIRP*, vol. 62, pp. 440–445, 2017.

[19] P. Patel and V. Chaudhary, “Delamination evaluation in drilling of composite materials–a review,” *Materials Today: Proceedings*, vol. 56, pp. 2690–2695, 2022.

[20] H. Ho-Cheng and C. Dharan, “Delamination during drilling in composite laminates,” *Journal of Manufacturing Science and Engineering*, 1990.

[21] K. Kerrigan, V. A. Phadnis, R. M’Saoubi, and R. J. Scaife, “Critical damage modes in high-performance drilling of carbon fibre reinforced epoxy composites,” *Procedia CIRP*, vol. 131, pp. 100–106, 2025.

[22] L. Heberger, B. Kirsch, T. Donhauser, S. Nissle, M. Gurka, S. Schmeer, and J. C. Aurich, “Influence of the quality of rivet holes in carbon-fiber-reinforced-polymer (cfrp) on the connection stability,” *Procedia Manufacturing*, vol. 6, pp. 140–147, 2016.

[23] A. Maghami, M. Salehi, and M. Khoshdarregi, “Automated vision-based inspection of drilled cfrp composites using multi-light imaging and deep learning,” *CIRP Journal of Manufacturing Science and Technology*, vol. 35, pp. 441–453, 2021.

[24] K. Matalgah, P. K. Ravindranath, D. Pulipati, and T. J. Fleck, “Automated quantification of interlaminar delaminations in carbon-fiber-reinforced polymers via high-resolution ultrasonic testing,” *Polymers*, vol. 15, no. 24, p. 4691, 2023.

[25] C. Niu, B. Chen, E. Smith, R. Bramley, P. Crawforth, M. Mahfouf, and V. Kadirkamanathan, “Pixel-based hole quality evaluation in robot drilling manufacturing process,” in *2024 IEEE 22nd International Conference on Industrial Informatics (INDIN)*. IEEE, 2024, pp. 1–6.

[26] A. C. Thompson, *Minkowski geometry*. Cambridge University Press, 1996.

[27] N. Chernov and C. Lesort, “Least squares fitting of circles,” *Journal of Mathematical Imaging and Vision*, vol. 23, pp. 239–252, 2005.

[28] M. A. Fischler and R. C. Bolles, “Random sample consensus: a paradigm for model fitting with applications to image analysis and automated cartography,” *Communications of the ACM*, vol. 24, no. 6, pp. 381–395, 1981.

[29] C. E. Duchon, “Lanczos filtering in one and two dimensions,” *Journal of Applied Meteorology (1962-1982)*, pp. 1016–1022, 1979.

[30] B. Jähne, *Digital image processing*. Springer, 2005.

[31] B. Chen, C. Niu, E. Smith, R. Bramley, P. Crawforth, M. Mahfouf, and V. Kadirkamanathan, “Spatial domain mapping from in-process sensor signals for visual inspection of multi-material stack drilling,” *Journal of Manufacturing Processes*, vol. 155, pp. 231–241, 2025.

[32] ——, “A novel spindle speed and angle estimation strategy in multi-material robotic drilling,” in *2024 IEEE 20th International Conference on Automation Science and Engineering (CASE)*. IEEE, 2024, pp. 1222–1227.

[33] C. Li, Y. Lei, L. Guo, E. Zio, H. Gao, and B. Yang, “GMM-BinSeg: A Data Segmentation Method for CFRP/Aluminum Stacks Drilling-Countersinking Monitoring Signal,” *IEEE Transactions on Instrumentation and Measurement*, 2024.

[34] X. Li, H. Wang, Y. He, and Y. Wang, “A Novel Methodology to Predict 3-D Surface Temperature Field on Delamination for Thermography,” *IEEE Transactions on Industrial Informatics*, 2024.

[35] X. Cheng, P. Chen, Z. Wu, M. Cech, Z. Ying, and X. Hu, “Automatic detection of CFRP subsurface defects via thermal signals in long pulse and lock-in thermography,” *IEEE Transactions on Instrumentation and Measurement*, vol. 72, pp. 1–10, 2023.

Chaoyue Niu received the M.Sc. degree in Robotics from King’s College London, U.K., in 2017 and the Ph.D. degree in Computer Science from the University of Southampton, U.K., in 2023. He is currently pursuing Post-Doctoral research at the University of Sheffield. His research interests include autonomous navigation in unstructured environments, multimodal sensing and in-process metrology in robotic and composite manufacturing, and acoustic and multi-modal analysis for pervasive healthcare monitoring.

Bin Chen received the M.Eng. degree in embedded system and the Ph.D. degree in electronics and computer science from the University of Southampton, Southampton, U.K., in 2017 and 2022, respectively. He is currently a Post-Doctoral Researcher with the University of Sheffield, Sheffield, U.K. His research interests include iterative learning control, analysis and control of large scale networked dynamical systems, signal processing, and analysis of manufacturing data.

Erica Smith received a BEng in Mechanical Engineering from the University of Bradford, UK, in 2014, while concurrently working in the automotive industry. In 2016, she joined the University of Sheffield Advanced Manufacturing Research Centre (AMRC) as a Project Engineer. She is currently a Technical Lead in Statistical Process Control for the AMRC. Her research interests include applied statistics for high volume manufacturing, and optimisation of cylindrical and centreless grinding processes.

Rob Bramley received an M.Eng. degree in mechanical engineering from the University of Sheffield, United Kingdom, in 2015 and is currently working towards a PhD in manufacturing engineering with the University of Sheffield. His current research focuses on technologies relating to hole generation, particularly for aircraft assembly applications.

Oliver Hayes is a Technical Fellow at The University of Sheffield AMRC. His research focuses on the subtractive manufacturing of carbon fibre reinforced polymer composite components. Particular research interests include characterization of material machinability, machining induced damage and the integration of physics informed machine learning into the manufacturing process.

Pete Crawforth is a Professor of machining at the University of Sheffield AMRC and leads the subtractive technology group which principally focuses on cross cutting low TRL (1-4) themes that bridge the gap between state-of-the-art subtractive processes and industry ready implementation strategies. His research brings a unique expertise to this project, bridging the gap between that of material science and machining.

Kevin Kerrigan received Ph.D. in Trinity College Dublin, Ireland, in 2013. He is currently a Professor (Chair) of Composite Manufacturing and Head of the Composite Centre at The University of Sheffield AMRC. He has spent the last 17 years producing world-leading research, utilising sensors to characterise process behaviours and responses of engineered composite materials during cutting and manufacturing operations.

Mahdi Mahfouf received the M.Phil. and Ph.D. degrees in control systems from The University of Sheffield, Sheffield, U.K., in 1987 and 1991, respectively. Since 2005, he has held a Personal Chair in intelligent systems engineering with The University of Sheffield (UK). He is the author of more than 360 papers, out of which more than 140 are journal papers. He has worked in the area of intelligent systems engineering, with a strong emphasis on fuzzy systems, modelling, control, and optimization for more than 35 years, with special applications to industrial systems and biomedicine. During this period, he had received several awards and prizes for his seminal work.

Visakan Kadirkamanathan received the B.A. degree in electrical and information sciences and the Ph.D. degree in information engineering from the Department of Engineering, University of Cambridge, Cambridge, U.K., in 1987 and 1992, respectively. He is currently a Professor in Signal and Information Processing and the Director of the Rolls-Royce University Technology Centre for Control, Monitoring, and Systems Engineering at Sheffield. He has published more than 300 papers in peer-reviewed journals and conferences. His research interests are in the areas of system identification, data-driven modeling, signal processing, and control with applications in aerospace, manufacturing, biomedical, and other dynamic systems. Dr. Kadirkamanathan was a recipient of the 2013 Proceedings of the National Academy of Science (PNAS) Cozzarelli Prize, USA. He is a past Associate Editor of the IEEE Transactions on Neural Networks, the Editor-in-Chief of the International Journal of Systems Science, among other conference and journal activities.